

Curved creases redistribute global bending stiffness in corrugations: theory and experimentation

Steven R. Woodruff · Evgueni T. Filipov

Received: 29 February 2020 / Accepted: 17 June 2020

Abstract Corrugations offer a convenient way to make thin, lightweight sheets into stiff structures. However, traditional, v-shaped corrugations made from straight creases result in highly anisotropic stiffness which leads to undesirable flexibility in some directions of loading. In this paper, we explore the bending stiffness of curved-crease corrugations with a planar midsurface – developable corrugations made by folding thin sheets about curves and without linerboard covers on the top or bottom. The curved-crease corrugations break symmetry in the pattern and can redistribute stiffness to resist bending deformations in multiple directions. To study these systems, we formulate a framework for predicting the bending stiffness of any planar-midsurface corrugation from its multiple geometric features at different scales. We use the framework to create two predictive methods that provide valuable insight to the global stiffness of corrugations without a detailed analysis. Results from these methods match well with experimental, three-point bending tests of five corrugation geometries made from polyester film. We found that corrugations with elliptical or parabolic curved-creases that intersect with one edge of the pattern are best at redistributing stiffness in multiple directions. While a straight-crease

pattern has a stiffness of about 4 [N/mm] in one direction and about 0 [N/mm] in the other, a parabolic crease pattern has a stiffness of about 2.5 [N/mm] in both directions. These curved-crease corrugations can enable the self-assembly and fabrication of practical, stiff structures from simple, developable sheets.

Keywords corrugations · curved-crease origami · lightweight structures · developable folding · multi-directional stiffness

1 Introduction

Corrugations are an essential geometric feature in a wide range of load-resisting applications. By deforming a flexible, thin sheet into a pattern of ridges and grooves using wrinkles or creases, the structure gains significant resistance to bending. Using the same amount of material as a plate, a simple corrugation can see an increase in stiffness of about three orders of magnitude [12]. Applications span many fields including: (1) civil engineering where corrugated roofs and floor slabs limit the dead weight of the structure while maintaining strength, stability, and serviceability, (2) packaging engineering with corrugated cardboard, (3) aerospace engineering where corrugated sandwich panels are used for lightweight wings, (4) mechanical engineering with examples like corrugated hoses and gaskets, and (5) ship decks designed by naval architects [3].

Corrugations are an example of lightweight, and therefore, efficient structures, but they are not without limitations. In their simplest form, corrugated structures are made by folding a flat, developable sheet along straight creases, which results in highly anisotropic bending stiffness behavior. Figure 1a shows an example of such a traditional, v-shaped corrugation made with straight creases. This geometry can resist bending about one direction (Figure 1b), but collapses when

The authors thank the Office of Naval Research for their financial support (Grant No. N00014-18-1-2015). The first author thanks the National Science Foundation Graduate Research Fellowship Program for their support (Grant No. DGE 1256260).

Steven R. Woodruff
University of Michigan;
Department of Civil and Environmental Engineering;
2350 Hayward St.; Ann Arbor, MI 48109; USA
E-mail: stevenrw@umich.edu

Evgueni T. Filipov (corresponding author)
University of Michigan;
Department of Civil and Environmental Engineering;
2350 Hayward St.; Ann Arbor, MI 48109; USA
Tel.: +1-734-764-8339
E-mail: filipov@umich.edu

loaded about another direction (Figure 1c). Prior research has addressed this limitation of corrugated structures in a number of ways. For instance, a traditional means of resisting compliant unfolding in roof structures is by supporting the edges with beams and columns at each valley crease [15]. Other means of restricting unfolding involve embedding a corrugation into a material matrix, like steel into concrete [8] or copper in tin [2]. Similarly, corrugations can be restrained using partial embedding on one side, similar to composite, concrete-metal decking [11].

Arguably, the most popular method to overcome the anisotropy and to improve the corrugation bending behavior is to sandwich it and connect it with two linerboards (for instance, corrugated cardboard [32] or sandwich corrugations [26]). Others have seen functionality in the stiffness anisotropy of corrugations and used them to design morphing structures [23][24][27]. Origami principles have also inspired new corrugation designs with tunable stiffness characteristics. Another benefit of origami is rapid fabrication from flat sheets through self-assembly [13]. Furthermore, origami tube [7] and arch [9] systems have been shown to increase stiffness while reducing global anisotropy.

The above solutions to stiffness anisotropy are limited, however. Additional supports complicate the design and might be unavailable for certain applications. Composite-embedded structures add additional weight to the corrugation that may be disadvantageous to a design. Sandwich corrugations complicate the design and manufacturing of the structure with additional adhesion between layers. Many straight-crease origami designs require locking mechanisms or complex, non-developable manufacturing. Although some origami-inspired corrugations may exhibit improved global ‘‘isotropy’’ (for example, miura-ori or egg box patterns), this improved isotropy comes at a great loss of global stiffness. For example, the strong direction of a traditional, v-shaped corrugation made with straight creases is over seventy-five times stiffer than the Miura-ori pattern [12]. It would be ideal if we could construct corrugations with stiffness isotropy, that are made from a simple, flat, developable sheet, and do not require added support or adhesion.

In this work, we introduce an origami-inspired, *curved-crease corrugation* that achieves this unique stiffness isotropy. The system is made from a thin, developable sheet, but instead of straight creases, curves are used to fold parabolic or elliptical corrugations into three-dimensional shapes that have a planar midsurface. Figure 1d shows an example of these curved-crease corrugations made from paper. This structure is stiff enough to resist significant loads in both directions (Figure 1e-f).

Curved creases have been used in origami for art [4] as well as in engineering contexts. These geometries have been studied mathematically, relating the crease geometry to the geometry of the folded sheet [5][14][18]. Additional

research has explored the folded geometries in terms of sheet deformations using elastica equations [20], finite element analysis [29][30], and energy minimization [1].

Early work on the structural properties of curved-crease corrugations explored their performance under impact [10]. Other research has suggested that curved-crease corrugations possess non-structural advantages such as improved performance for gas or fluid transport [16][17]. Existing research has not identified the unique stiffness isotropy possible with curved-crease sheets. Additionally, there is currently no framework or method to predict or estimate the bending stiffness of such corrugations.

In this paper, we present a theoretical framework and experimental data to show the unique bending stiffness properties of curved-crease corrugations. The format of the article is as follows. In Section 2, we describe a framework for qualitatively connecting geometric characteristics of a corrugation to its bending stiffness about any direction in the xy -plane. In Section 3, we present the geometries of five origami corrugation patterns used in subsequent analyses and experiments. In Section 4, we use two methods to quantitatively predict the bending stiffness of the folded, three-dimensional corrugation geometries estimated using a bar and hinge analytical simulation. In Section 5, we present three-point bending tests of physical corrugations made from polyester film and compare the results to the predictions made in Section 4. Conclusions and discussion of future work are presented in Section 6.

2 Stiffness contributions at multiple scales

When considering a corrugated system for structural function, we often want the system to support external loads while minimizing the overall displacement. Consider a thin, isotropic, homogeneous rectangular plate lying in the xy -plane with applied loads that cause a small deflection, w , in the z -direction and internal bending moments per unit width, M_x , M_y , and M_{xy} . The moment-curvature relationships for this plate are

$$M_x = D \left(\frac{\partial^2 w}{\partial x^2} + \nu \frac{\partial^2 w}{\partial y^2} \right); \quad (1)$$

$$M_y = D \left(\frac{\partial^2 w}{\partial y^2} + \nu \frac{\partial^2 w}{\partial x^2} \right); \quad (2)$$

$$M_{xy} = -D(1 - \nu) \frac{\partial^2 w}{\partial x \partial y}, \quad (3)$$

where $D = Eh^3/[12(1 - \nu^2)]$, E is the elastic modulus of the plate material, h is the thickness of the plate, and ν is the Poisson’s ratio [28]. If we assume, for simplicity, that $\nu = 0$ and that a line load is applied that causes bending about the y -direction (without loss of generality), the moment-curvature relationships reduce to that of a beam with a bending moment

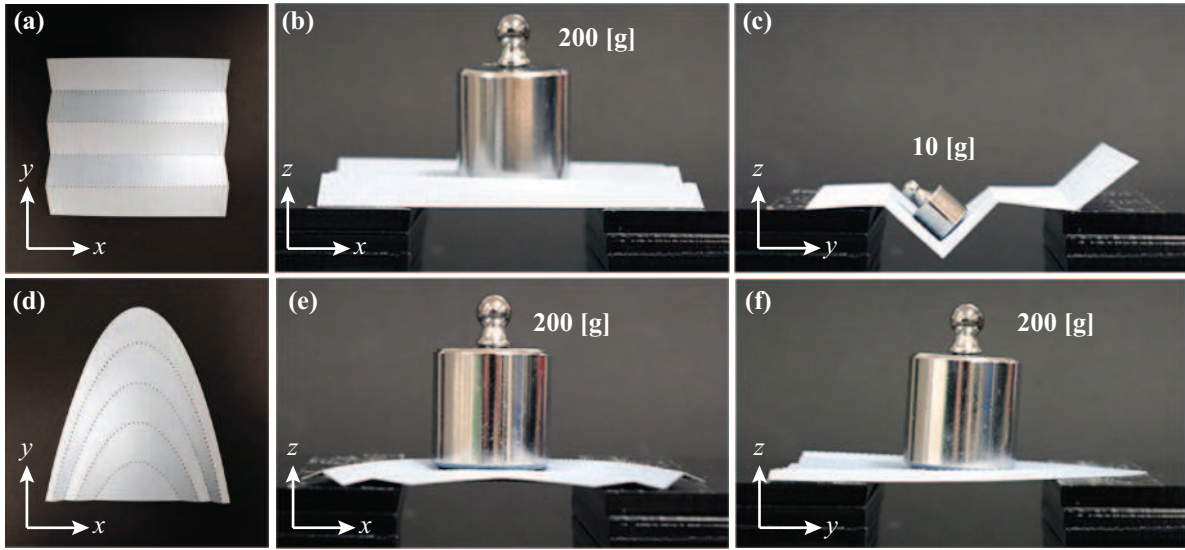


Fig. 1 Not all corrugated systems are the same. (a) A v-shaped, straight-crease corrugation (b) can support 200 [g] in bending about the y -direction, but (c) collapses when carrying 10 [g] in bending about the x -direction. (d) A parabolic, curved-crease corrugation supports 200 [g] in bending about both the (e) y -direction and (f) the x -direction.

about the y -direction, M , that varies along its length in the x -direction, but is constant across its width, b . That is,

$$M = EI \frac{d^2 w}{dx^2}, \quad (4)$$

where $I = bh^3/12$ is the second moment of area about the y -direction. Through double integration over the length of the plate and application of boundary conditions, the deflection can be calculated from Equation 4.

When corrugations are folded into geometries with a flat midsurface and applied loads are unidirectional, the corrugation's deflection should behave similarly to that of a plate. If we keep the boundary and loading conditions the same between different corrugation geometries and maintain the same homogeneous material properties of the sheet, the second moment of area should be the only structural property that changes with the corrugation geometry. Given the complex geometry of a folded corrugation, the exact second moment of area will be heterogeneous and will depend on the location in the corrugation's xy -plane. Through careful consideration of the corrugation's folded geometry, we can simplify the second moment of area into one averaged value, and subsequently, simplify the deflection analysis.

In this section, we examine planar-midsurface corrugation systems created by folding about arbitrarily oriented creases and identify how variations in the geometry affect the bending stiffness of the structure. We organize the observations as a framework that considers the geometry at multiple scales, including the basic sheet section, unit cross-section, a single crease, and the entire corrugated system (Figure 2a). The qualitative geometric framework is then used to formulate two methods for predicting the averaged

second moment of area value, and thus, the stiffness of an arbitrary curved-crease geometry.

2.1 Sheet section

If we break down the geometric characteristics of a creased corrugation, the smallest relevant property is the stiffness of the sheet section spanning between creases (Figure 2a(i)). Bending the sheet section over its length, s , can first be characterized by its second moment of area

$$I_{\text{sheet}} = \frac{\omega t^3}{12(1 - \nu^2)}, \quad (5)$$

where ω is the width of sheet under consideration (into the page), t is the thickness of the sheet, and ν is Poisson's ratio of the material. Here, we assume that the width of the sheet, ω , is much greater than s , which makes the bidirectional Poisson's effect important for considering sheet bending. This second moment of area for the sheet is a function of thickness cubed. Considering that the sheet thickness is small, this relation shows that bending between creases is overly flexible, and thereby unwanted in the overall corrugation. Another important geometric quality of the section stiffness is the spacing between creases, s . Similar to the importance of length to a beam in bending, the crease spacing affects the ability of the sheet to resist local bending. A larger crease spacing will give a longer, unsupported span that will bend more easily than a smaller crease spacing.

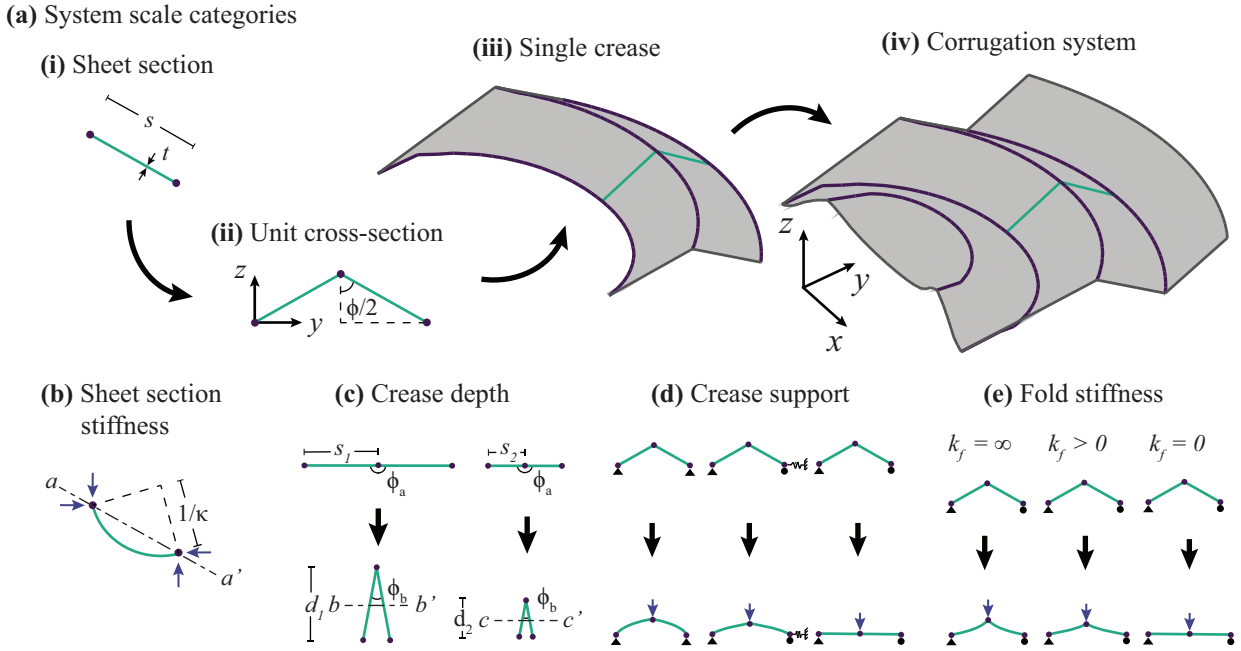


Fig. 2 (a) The stiffness of a corrugation depends on its geometric properties at multiple scales combined into the full system. (b) Sheet section stiffness for bending about its original plane ($a-a'$) is the most local property giving stiffness to a system. (c) Crease depth adds bending stiffness about directions in the xy -plane by distributing material away from the neutral axes ($b-b'$ and $c-c'$). (d) The supports at the edges of a unit cross-section affect the stiffness as well as the crease's ability to resist flattening and large deformations. (e) Similarly, fold stiffness gives the unit cross-section stiffness to resist flattening and determines whether the sheet or the crease will deform more.

2.2 Unit cross-section

The next scale we consider is the unit cross-section defined at each point along the length of the crease (see Figure 2a(ii)). Here, we consider bending to occur orthogonal to the cross-section (about $b-b'$ and $c-c'$ in Figure 2c); therefore, the folded unit cross-section redistributes material away from the neutral axis. The unit cross-section has two important qualities that contribute to how it redistributes material, and thereby, how much it increases the global bending stiffness of the corrugation. The first quality is the depth of the unit cross-section and the second is how well it maintains its folded shape.

The depth of the unit cross-section is the distance between the top crease and the lower creases. The bending stiffness of a cross-section – in this case, about the cross-section's centroid in an xy -direction – increases as material is moved away from the neutral axis. The deeper the cross-section, the greater its second moment of area and the greater its bending stiffness will be. The second moment of area of half of the unit cross-section (one rectangular sheet) is

$$I_{\text{rect}} = \frac{st}{12} \left(s^2 \cos^2 \frac{\phi}{2} + t^2 \sin^2 \frac{\phi}{2} \right), \quad (6)$$

where ϕ is the fold angle (see Figure 2a(ii)). If additional sheets are to be taken into account, a new neutral axis can be computed, and the total second moment of area can be found using the parallel axis theorem.

Because $s \gg t$, the bending stiffness of the unit cross-section is mostly dependent on two important parameters, s and ϕ . Increasing s will increase the depth of the unit and result in a larger bending stiffness (Figure 2c). Additionally, the more a unit cross-section is folded ($\phi \rightarrow 0$), the greater its depth (within the domain $0 < \phi \leq \pi$ [rad]). However, from a practical perspective, it is not useful to have overly folded creases because the surface area covered by the corrugation would go to zero. In a general sense, the unit cross-section bending stiffness is going to be much greater than the section bending stiffness because the way in which the sheet is loaded. For bending about the unit cross-section, the upper portions of the corrugation will carry compression while the lower portions will carry tension, or vice versa. In this scenario, bending of the actual sheet is avoided and the structure is much stiffer.

It is important for a unit cross-section to maintain its folded shape during loading, because if it flattens, its depth will be reduced, and the overall stiffness of the corrugation will decrease. The boundary conditions surrounding the unit cross section, the local crease stiffness, and the sheet section stiffness will all affect the ability of the system to maintain its shape. The boundary conditions or supports surrounding the unit-cross-section are dependent on the adjacent creases in the corrugation and will likely fall between a case with two fully pinned ends and a case with a pin and a roller support (Figure 2d). In curved-crease corrugations, the different geometry of separate creases will lead to stiffer boundary

conditions for each individual crease. Next, a high crease stiffness, k_f , will also maintain the folded shape better, regardless of the boundary conditions. Creases in corrugations often have lower stiffness than the base sheet because of intentional damage during the fabrication (for instance, perforation). In some cases however, plastic deformation and strain hardening of the creased material can lead to a stiffer crease than the base material. Finally, the sheet section bending behavior as discussed in Section 2.1 will also have an effect in the unfolding of the corrugation during loading (see cases with high fold stiffness in Figure 2e) [19].

2.3 Single crease

The next geometric scale we consider is the single crease shown in Figure 2a(iii). The single crease connects two continuous sheets together, and forms a full, three-dimensional, beam-like structure. The first geometric quality to consider for a single crease is the unsupported length or distance that it spans. The longer this distance, the more flexible the full system would be. Furthermore, we assume that creases will continuously span through the entire, or at least through most of the corrugation. Although it may be possible to interweave multiple creases that together form a span, we expect that the transfer locations that connect creases will result in weak points susceptible to bending.

The next important geometric characteristic is the directionality of the crease. Straight creases, such as those in the Figure 1a will have a high second moment of area in one direction, but will not be able to provide stiffness in orthogonal directions. In contrast, a curved crease will reorient the unit cross-section over its length, and can thereby provide additional stiffness to the structure in multiple directions. The curved-crease approach can accomplish this cross-section reorientation with only one crease and does not require the introduction of additional creases, or any external stiffeners. Indeed, a straight-crease geometry like a hornbeam leaf (sometimes modeled as a row of Miura-ori units [22]) has greater directionality than a traditional, v-shaped corrugation, but gains flexibility from the additional creases. Moreover, bending stiffness would still concentrate around the few directions perpendicular to the crease. Note, however, that the curved creases also introduce a fundamental problem to the overall beam-like crease structure because the system becomes asymmetric. If the crease is loaded in the center and supported at the ends, then this asymmetry will result in combined bending and torsional deformations, which would make the structure substantially more flexible than a straight crease design. In the next subsection, we discuss how the full corrugation design can reduce these unintended torsional deformations.

2.4 Corrugation system

The corrugation brings together the geometric properties from multiple scales into one interdependent structural system. It should span a distance and be stiff regardless of how it is oriented. We consider a corrugation made from a single, developable sheet where no external components or constraints are used to stiffen the structure. The geometry of the crease pattern can directly give insight to some of the stiffness characteristics. Creases that are placed close together would result in a smaller depth and smaller second moment of area. However, creases that are spaced far apart may leave large regions of the sheet unrestrained, which could result in unwanted and flexible deformations of the sheet section (Figure 2b). Greater folding of the corrugation typically leads to a deeper section and a higher second moment of area; however, the amount of folding also needs to consider the desired geometry (for instance, final surface area). The ability of the corrugation to maintain its folded state (and thereby, stiffness) during loading will depend on the crease stiffness, the sheet section stiffness, and the intrinsic boundary conditions that restrain each crease. We have observed that curved-crease corrugations with different crease geometries provide better restraint to prevent unfolding and flattening. Curved creases are important for reorienting the cross-section to provide multi-directional stiffness for the corrugation. The curved creases should have a large enough change in directionality such that the depth of the cross-section covers multiple axes (for instance, a change of more than 120°). When placing multiple creases together, it is beneficial to use creases with different geometries such that they can counteract torsional deformations of each individual crease. The curved creases can vary in both curvature and general shape.

3 Corrugation geometries

In order to compare and analyze the effects of curved creases on the bending stiffness of a planar-midsurface corrugation, we chose five different crease patterns to explore. Each corrugation starts with the following assumptions for its flat crease pattern: (1) the origin of the coordinate system lies at the lowest vertical point in the pattern and at the middle horizontal point, (2) the pattern is symmetric about the y -axis (this helps ensure the folded shape has a planar midsurface), (3) the longest part of the pattern in the x -direction lies on $y = 0$ and has length W , (4) the longest part of the pattern in the y -direction lies on $x = 0$ and has length H , (5) the pattern has n_f creases and $n_s (= n_f + 1)$ sheets between creases or between a crease and an edge, and (6) the curves are defined by one-to-one functions in the x -domain. These assumptions do not include all possible corrugation patterns, but limits the scope of the analysis.

Each of the five models we chose displays different geometric features that theoretically change the bending stiffness of the corrugation and allows for insights about how key qualitative parameters laid out in Section 2 affect the bending stiffness of the corrugation. Key qualitative parameters include the diversity of a crease's tangent directions and the depth of the cross-section throughout the structure. By folding physical models and running numerical simulations of folding (described in Section 4.1), we know that each model folds with little to no stretching deformation, does not intersect itself in the tested range of folding, and does not display buckling out-of-plane or other unstable behavior.

Each crease pattern starts with a zeroth curve that is just a line segment defined as $y_0 = 0$ on $-W/2 \leq x \leq W/2$. The curves y_1 through y_{n_s} are defined based on the specific geometry being used. Starting with the base constraining assumptions, the following crease patterns and resulting corrugations are constructed.

Straight-crease corrugation The straight-crease corrugation serves as the baseline geometry for a traditional corrugation design with a v-shaped cross-section, which we then use to compare the different curved-creased designs. The geometry has only one input beyond the constraining assumptions. This pattern is shown in Figure 3a.

Parabolic-point corrugation The parabolic-point corrugation is constructed using parabolic curves that share roots. Because the curves meet at a point, the creases are easy to restrain (for instance, using a pinned connection at the root). However, because the curves meet at a point, the spacing between the creases decreases near the root, which reduces the corrugation depth. The parabolic geometry has two inputs beyond the constraining assumptions. This geometry is shown in Figure 3b.

Parabolic-edge corrugation The parabolic-edge corrugation is constructed by shifting the y_{n_s} curve of the parabolic-point corrugation down an equal spacing, H/n_s . In this pattern, the creases do not terminate at the same point, which makes the pattern more prone to unfolding. However, the depth of the corrugation is more consistent across the pattern. Similar to the parabolic-point, this geometry has two inputs beyond the constraining assumptions. This crease pattern is shown in Figure 3c.

Elliptical-point corrugation The elliptical-point corrugation is constructed using positive y -value, elliptical curves that share roots and have semi-axes aligning with the x - and y -axes. The elliptical shape has a larger area underneath the curve than the parabola, giving a larger surface area for the corrugation. Furthermore, the elliptical shape is beneficial in that the roots give vertical folds (aligned with the

y -axis) which gives greater resistance to bending about the x -direction near the bottom edge. However, the elliptical shape has low curvature near $x = 0$ which could reduce the corrugation's ability to resist bending about the x -direction in other parts of the corrugation. Similar to the parabolic-point, the elliptical-point corrugation will resist unfolding at the roots with fewer restraints, but will have less depth near the roots. The geometry has three inputs beyond the constraining assumptions and is shown in Figure 3d.

Elliptical-edge corrugation The elliptical-edge corrugation takes the y_{n_s} curve of the elliptical-point corrugation and shifts it down a spacing, H/n_s . Like the parabolic-edge corrugation, depth is better preserved with this pattern, but the system becomes more prone to unfolding. The geometry has three inputs beyond the constraining assumptions and is shown in Figure 3e.

These five crease patterns are used in the following sections. Further details on the functions used to generate the curves and the geometric values used in the physical models and bar and hinge simulations are presented in Appendix A. We later predict the bending stiffness of these corrugations and verify the prediction with experimental, three-point load tests.

4 Predicting bending stiffness from the folded shape

Given a flat crease pattern, one could estimate the bending stiffness of the folded corrugation using the framework presented in Section 2. For a geometry like the straight-crease model, the depth of the structure, the sheet section stiffness, and the effects of boundary restraints are easy to predict, and thus, the stiffness can be inferred. For more complicated geometries, like the curved-creased corrugations, there is greater variation in the spacing between the curves and the fold angles that minimize strain energy in the sheets. This makes the process of surmising the folded bending stiffness from the flat crease pattern prohibitively challenging.

In order to simplify the process of predicting the bending stiffness of a folded corrugation, we offer two methods that employ a bar and hinge simulation to find the folded shape of a flat crease pattern and calculate quantitative metrics for bending stiffness. In both methods, the quantitative metric is analogous to the average second moment of area of the cross-sections of the corrugation. In beam bending, the second moment of area is used to describe the variation of area in a cross-section about its centroid, which is associated with resistance to strains in an elastic beam. Since a folded corrugation does not have the same cross-section across its length, the average second moment of area only gives an approximate way of predicting the bending stiffness of the system. Additionally, the methods we present only look at

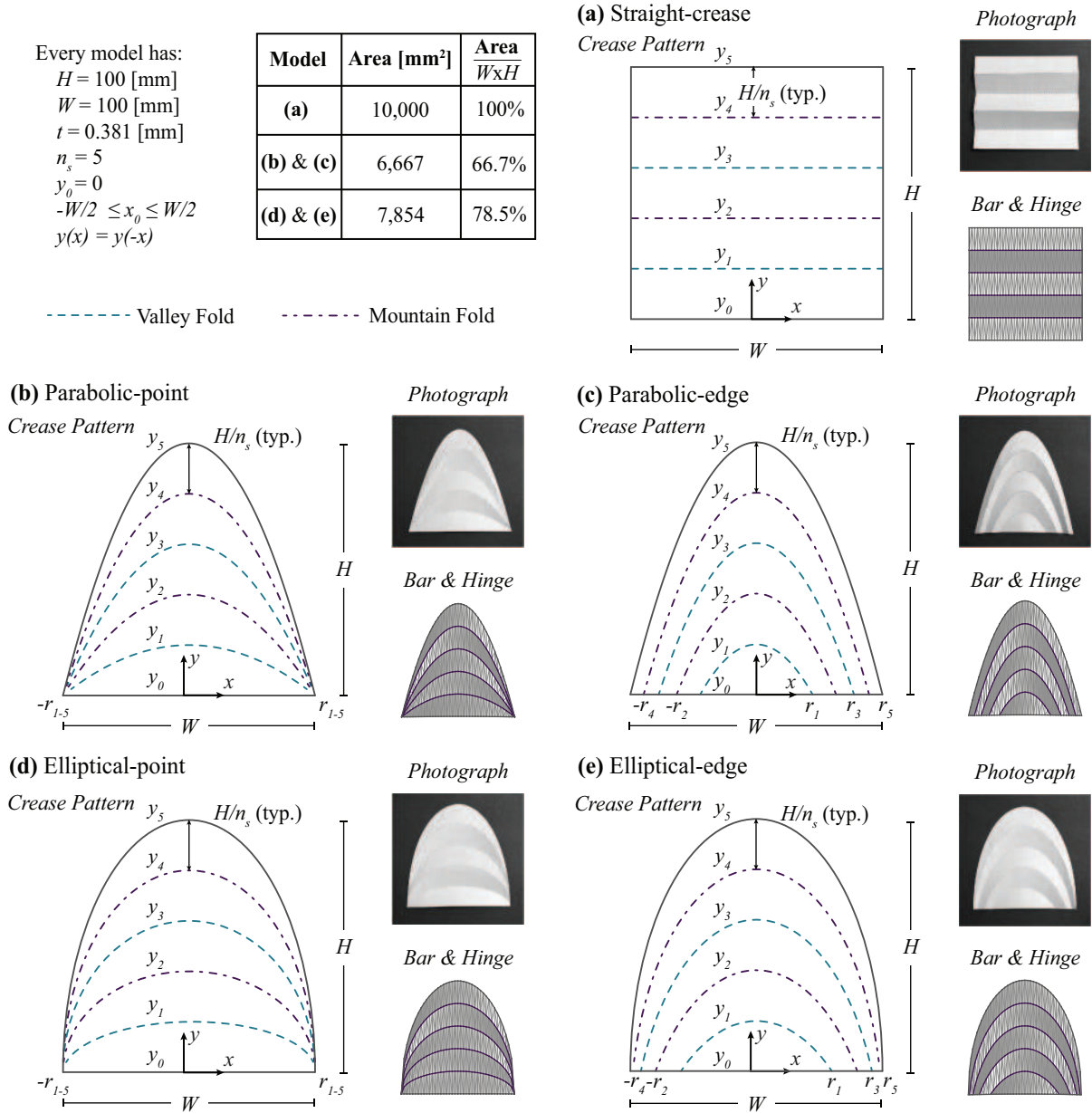


Fig. 3 Five corrugations with flat crease patterns, folded paper specimens, and folded bar and hinge simulations. The geometries used in subsequent analysis are: (a) the straight-crease geometry, (b) the parabolic-point geometry, (c) the parabolic-edge geometry, (d) the elliptical-point geometry, and (e) the elliptical-edge geometry.

the geometry of the folded shape which ignores the effects of fold restraint. Despite these limitations, we found that these methods for predicting the bending stiffness offer key insights into the performance of the structure without having to run physical tests or high-fidelity finite element models.

4.1 Bar and hinge method for estimating folded shape

The bar and hinge method is a simplified, physics-based simulation tool that takes a flat crease pattern, material properties, boundary conditions, and prescribed fold angles

and simulates the folding sequence of the thin sheet system [6][25]. The bar and hinge method is able to capture complex, mechanical behavior such as in-plane deformations and geometrically nonlinear stiffness responses using input similar to finite elements [21]. Although originally designed for straight-crease origami analysis, a modified bar and hinge method simulates the folding of curved-crease origami and can estimate the folded shape of patterns with many creases [31].

The bar and hinge method works by describing the geometry and deformation response with three element types: (1)

bars that capture in-plane deformations, (2) bending hinges that capture sheet bending, and (3) folding hinges that capture crease rotations. The force-deformation response is affected by the stiffness of each element which is calculated using the geometry of the crease pattern and the material properties prescribed to the model. Folding is achieved by prescribing a rest angle to rotational springs about the crease (that is, the angle at which each crease is strain-free). The bar and hinge method then minimizes the strain energy in the system and converges to a folded state. Because the bar and hinge method uses few degrees of freedom, simulations take much less time to run than traditional shell modeling with finite elements. Furthermore, bar and hinge modeling of curved-crease origami captures folding without the convergence issues often seen in finite element modeling. Our prior work on this simulation approach showed its validity for capturing the folding behavior of curved-crease origami similar to the parabolic-edge corrugation [31]. The origami geometry simulated with the bar and hinge model was compared to a physical model folded by hand, and the Hausdorff distance between the two had an average error of 0.4% of the maximum length of the model. Given these qualities, the bar and hinge method can be used to quickly predict the folded shape, and can thereby be used in the two predictive methods described in Sections 4.2 and 4.3.

For each of the five crease patterns, we ran bar and hinge simulations to find the folded shape. The material properties are defined to be those of the polyester film used to make physical specimens for the experimental study in Section 5. Each model was folded such that the depth of the corrugation, calculated as the difference between the highest point of the mountain creases and the lowest point of the valley creases in the z -direction, was identical. These three-dimensional folded shapes are then analyzed using the two methods for quantifying the stiffness of the corrugation.

4.2 Top-down method

The first procedure that we propose for predicting the bending stiffness of a folded corrugation is called the top-down method. In this procedure, we investigate the entire corrugation as a whole, and evaluate the cross-section at different points along the span of the corrugation. Starting with the three-dimensional folded shape of the corrugation, we pick a direction, d , in the xy -plane, which we will consider as the span direction (Figure 4a). The cross-section of the corrugation in the perpendicular direction ($d \perp$) is then used to compute the second moment of area, $I_{d\perp}$, with a sheet thickness used in the later experimental tests, $t = 0.381$ [mm] (Figure 4b). The cross-section is divided into segments, the neutral axis is found, and Equation 6, together with the parallel axis theorem, are used to find $I_{d\perp}$.

Figure 4b shows how the second moment of area in the d -direction of the parabolic-edge corrugation varies along the length of the span. Peaks in $I_{d\perp}$ correspond to portions of the corrugation with large and deep cross-sections, while low points correspond to smaller and shallower cross-sections. At the ends of the span, the cross-section size and resulting $I_{d\perp}$ approach zero. This distribution of bending rigidity along the span is similar to conventional tapered beam designs that have a smaller depth where the bending moments are lower. Under three-point bending, the normalized curvature $k = M/I_{d\perp}$ (without an elastic modulus) tends to be low until the ends of the span where $I_{d\perp}$ approaches zero. For a practical application, we can assume that those ends of the corrugations will be supported vertically, and will not experience any moments.

The average of the second moments of area is taken for the central 80% of the span to provide a single quantitative value, $\bar{I}_{d\perp}$, for the corrugation in the given direction, d . This averaged value for second moment of area can then be presented for all directions in the xy -plane as a polar plot where distance from the centroid represents a higher magnitude (Figure 4c). Polar plots for all five models are shown in Figure 4d. As expected, this procedure shows that the straight-crease pattern has a high rigidity for bending about the y -axis, but a low bending rigidity for bending about the x -axis. About the x -axis, the second moment of area is $\bar{I}_{d\perp} = Wt^3/12 = 0.461$ [mm⁴], which implies just bending of the thin sheet. The curved-crease corrugations have higher second moments of area regardless of the direction, and there is never a case where the cross-section is entirely flat in the xy -plane.

4.3 Bottom-up method

The second procedure for predicting the bending stiffness of a folded corrugation is called the bottom-up method. This procedure involves analyzing the corrugation at discrete points along the length of the mountain creases, calculating a second moment of area for that local area, and averaging the set of values across the entire corrugation.

The bottom-up procedure relies on the discretization of the corrugation such that each mountain crease bar (folding element within the bar and hinge model) represents the size of the sheet locally. Figure 5a shows a representation of the parabolic-edge corrugation. With this crease pattern, there are two mountain creases (shown as a dark line within the corrugation). Figure 5b shows the corrugation divided into discrete bars extending between points (for example, between p_i and p_{i+1}). Each bar coincides with a vector, \mathbf{T}_i , that is roughly tangent to the folded crease at that point. The portion of this vector lying in the xy -plane is inclined an angle, θ_i , from the x -axis. We treat this portion of the tangent vector as the normal vector to a plane in which the z -axis lies.

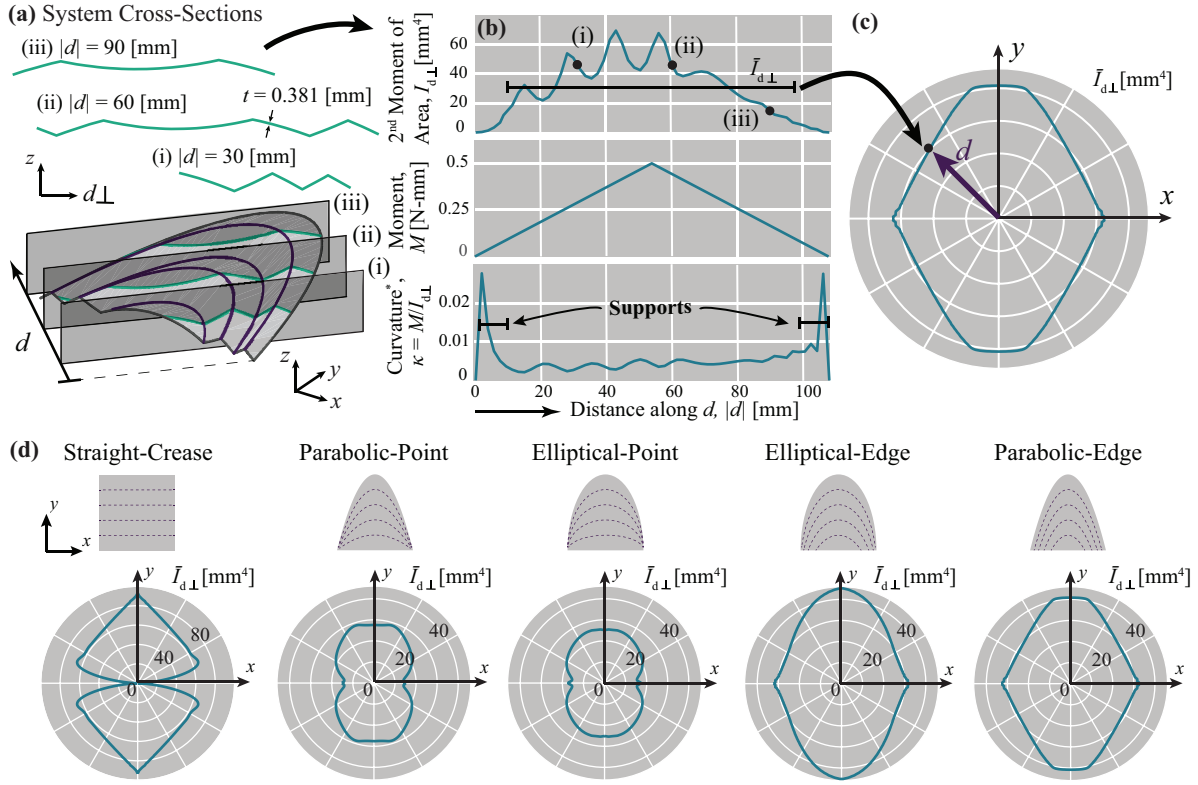


Fig. 4 (a) The cross-section geometries perpendicular to the direction d are obtained for multiple points (for example, (i), (ii), and (iii)) over the span of the folded corrugation. (b) The cross-sections are then used to compute the second moment of area $I_{d\perp}$ along the distance of d . If an applied moment from a three-point bending is considered over the entire span, then most of the normalized curvature (*with no elastic modulus) would occur at the ends of the corrugation; thus, we assume the ends are supported. (c) The second moment of area is averaged over the central 80% of the span for all directions in the xy -plane and is presented as a radial plot. (d) $\bar{I}_{d\perp}$ for all directions in the xy -plane for the five corrugation models.

This plane, defined by the coordinates z and $z \times \mathbf{T}_i$ (where “ \times ” is the cross product), defines the surface on which the two-dimensional unit cross-section shown in Figure 2c lies.

The next step in the bottom-up procedure involves finding the intersection between that plane and the two adjacent valley fold bars. The vectors \mathbf{S}_i^L and \mathbf{S}_i^R originate at the point p_i and extend to those intersection points. The unit cross-section shown in Figure 5c represents the local cross-section of that crease. Using Equation 6, we can calculate the second moment of area of each sheet section, I_i^L or I_i^R , of the local cross-section where $s = s_i^L = |\mathbf{S}_i^L|$ or $s = s_i^R = |\mathbf{S}_i^R|$ and t is the prescribed thickness of the sheet (0.381 [mm]). The dihedral angle, $\phi = \phi_i^L$ or $\phi = \phi_i^R$, is calculated for each sheet section. We sum the second moment of area for each sheet section to get the local second moment of area, I_i^{loc} . Because the length of each local mountain crease bar might vary, we weigh the local second moment of area by the length of the bar, $L_i^f = |\mathbf{T}_i|$, divided by the length of all the mountain crease bars, $\sum_{j=1}^{n_{mf}} L_j^f$, where n_{mf} is the number of mountain fold bars in the bar and hinge model. The local

second moment of area for the i^{th} mountain crease bar is computed as

$$I_i^{loc} = \frac{L_i^f}{\sum_{j=1}^{n_{mf}} L_j^f} (I_i^R + I_i^L). \quad (7)$$

This expression represents the ability of the local unit cross-section to resist bending about the $z \times \mathbf{T}_i$ direction. In order to predict the corrugation’s ability to resist bending about another direction, we can find the projection of the local second moment of area onto that direction. We calculate the local second moment of area projected onto the x - and y -directions and sum them to find a single value for the corrugation using

$$I_x^{loc} = \sum_{i=1}^{n_{mf}} |I_i^{loc} \sin \theta_i|; \quad (8)$$

$$I_y^{loc} = \sum_{i=1}^{n_{mf}} |I_i^{loc} \cos \theta_i|. \quad (9)$$

We can then project these values onto any direction, $\mathbf{d} = [\cos \alpha \ \sin \alpha]$, in the xy -plane angled, $\alpha \in [0, \pi/2]$ [rad] from the x -axis using

$$I_{\mathbf{d}}^{loc} = [I_x^{loc} \ I_y^{loc}] \cdot \mathbf{d} = I_x^{loc} \cos \alpha + I_y^{loc} \sin \alpha. \quad (10)$$

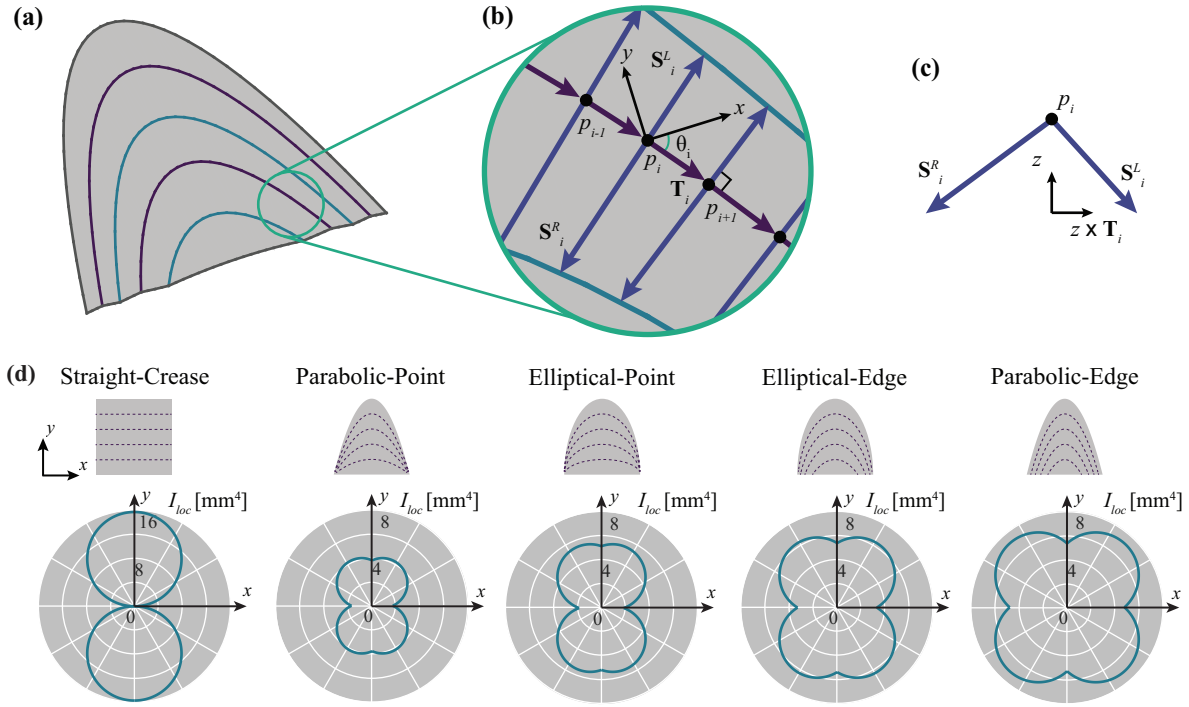


Fig. 5 The process for calculating local second moment of area starts by looking at (a) the mountain creases of a folded corrugation. (b) For each division of the crease (bars), we find the tangent to the crease, \mathbf{T}_i , at the mid-point, p_i , and (c) calculate a vector in the tangent plane to the adjacent valley creases, \mathbf{S}_i^L and \mathbf{S}_i^R . The resulting vectors are used to generate inclined rectangle cross-sections and we calculated the local second moment of area of each rectangle. We normalized and averaged these values, I_{loc} , for each model and calculated the projection of each unit cross-section second moment of area onto the x - and y -axes using θ_i . (d) I_{loc} is presented for each model folded to the same corrugation depth about all directions in the xy -plane.

We assume that bending about \mathbf{d} is equivalent to bending about $-\mathbf{d}$ and exploit the symmetry of the given models about the y -axis in this formulation.

The local second moment of area is calculated at each point along the length of the mountain creases. Portions of the model are excluded from this summation to account for restrained portions of the structure. We calculated the local second moment of area for each of the five specimen models with boundary conditions similar to those in the physical tests described in Section 5. These values are shown in Figure 5d. We see that the results are similar to those found in the top-down method shown in Figure 4d. Because of the weighing factor and different approach to the methods, the values are different, but the relative magnitudes are similar. We next compared these prediction results to the results of experimental tests on physical corrugation specimens.

5 Three-point bending tests of corrugations

In this section, we describe and assess experimental load-deformation tests on corrugations made from polyester film sheets using the crease patterns described in Section 3. The experimental tests were designed to assess the stiffness of the corrugations in bending about the x -, xy - (the direction an-

gled 45° from the x -axis), and y -axes. We conducted these tests to address two main points. The first purpose was to demonstrate that curved-crease corrugations reduce the difference in stiffness between the weakest bending direction and the strongest, effectively allowing the corrugation to behave more like an isotropic plate than a highly orthotropic structure. The second purpose was to demonstrate that the qualitative framework presented in Section 2 used to create the quantitative predictions for stiffness found in Section 4 is suitable for predicting the stiffness of the corrugations. The experiments aimed to reduce the complexity of the framework by making all specimens with the same material properties, thickness, corrugation depth, and similar boundary conditions.

5.1 Experimental setup and procedure

Each of the five corrugation specimens were designed and fabricated using the flat crease patterns described in Section 3. The pattern was drafted in a computer-aided design software, and then cut into Graphix Dura-Lar polyester film sheets using a laser cutting machine. We chose this material because of its predictable material properties, its ability to undergo large deformations without permanent damage, and

for its ability to hold folded shapes mostly due to plastic damage in the creases after folding. The sheets were 0.381 [mm] (0.015 [in]) thick, and each corrugation was folded by hand such that the final depth, defined as the distance between the highest point along the mountain creases and the lowest point along the valley creases, was approximately 6 [mm] deep. Each of the five crease patterns was cut and folded three times, giving three samples for each corrugation.

The corrugations were loaded using a Mark-10 test stand (ESM1500FG) and force gauge (M5-50) (see Figure 6). The load cell had a resolution of 0.05 [N], which is less than 1% of the maximum load carried by the specimens. Displacement of the specimen was measured by the machine, and the magnitudes were verified using camera recordings. The forces for these tests are low, and deformation within the equipment is negligible compared to the specimen. The folded corrugations were placed on top of two aluminum supports which gave an unsupported span of 50 [mm]. Double-sided tape applied to the top of the aluminum supports held the corrugations in place and limited unfolding early in the loading process. The corrugations were aligned on the aluminum supports using guides that pointed to the center of the specimen. The corrugations were placed in one of three directions: x , xy , or y , which correspond to orientations of the load bar relative to the corrugation coordinate system. The load bar was 10 [mm] wide and made out of an acrylic sheet. The load bar was designed to allow for rotations with minimal friction at the connection to the load transfer box (an acrylic box that connects to the force gauge). The rotations allowed the bar to come into contact with multiple mountain creases on the corrugation without generating a notable axial force at the load cell. At the load transfer box, loosely attached clamps were used to prevent the bar from sliding along the dowel between the two supports.

A displacement-control test was conducted at a rate of 3.0 [mm/min]. Collection of the load data started when a trigger load of 0.10 [N] was measured to ensure that the load bar made full contact with the mountain creases. The load-displacement data was recorded at a sampling rate of three points per second for the duration of the test.

The displacement was carried out for 10 [mm] after the trigger load was measured. During the displacement-control test, we observed four stages of behavior. These stages demarcate the start and end points of where the data was analyzed to calculate the stiffness of the structure (see Figure 7). The first stage involves partial contact between the load bar and the mountain creases of the corrugation, and thus, the stiffness is low. Once the load bar has rotated to the point where full contact is made with multiple mountain creases, the stiffness rises. This stage is used to calculate the bending stiffness of the corrugation, k . As loading continues, the bar might come into contact with other parts of the corrugation (Figure 7b). This ends the stiffness extraction stage and starts

a period of increased stiffness due to greater participation of the material in resisting loads. This stage continues until one of the mountain creases flattens, resulting in a loss of stiffness (Figure 7c). The last stage involves large bending deformations with low stiffness due to the corrugation progressively becoming flatter (Figure 7d).

In the second stage, the load-deformation data is more-or-less homoscedastic (that is, the data surround a linear trend line with small variance). Using linear regression, the slope of the trend line can be calculated which represents the stiffness of the corrugation in the downward direction. Because the ratio of the depth of the corrugation to the unsupported span is about 12%, we can assume that the corrugation is slender and that the deformation in this stage is mostly due to bending about the direction parallel to the load bar. The stiffness extraction process was repeated for each of the three samples of the five corrugations in the x -, y -, and xy -directions, resulting in a total of 45 tests and analyses. The R^2 value of each analysis was always greater than 0.95 with most analyses exceeding 0.98, which suggests that the data closely fit with the linear model. We found the average of the slopes of the trend lines (that is, the average of the stiffness values) from the three samples in one load direction for each corrugation, which we call the stiffness of the structure, k . Load-displacement results from the experimental tests that were used to find the stiffness values are shown in Figure 8.

5.2 Experimental results and discussion

The five corrugation geometries in Figures 4, 5, 8, and 9 are ordered based on the ratio of the stiffness in bending about the x -direction, k_x , to the stiffness in bending about the y -direction, k_y , for the average values from the experimental data. This ratio, k_x/k_y , is one way of describing the corrugation's ability to resist bending in multiple directions. The closer the ratio is to 1, the more isotropically the corrugation behaves. As predicted, the experimental results show that the ratio for the straight-crease specimen is the lowest, $k_x/k_y = 3.74\%$. For the parabolic-point specimen, the ratio is, $k_x/k_y = 56.1\%$. For the elliptical-point specimen, $k_x/k_y = 58.0\%$. For the elliptical-edge specimen, $k_x/k_y = 70.5\%$. The parabolic-edge specimen had the largest ratio, $k_x/k_y = 93.4\%$.

Figure 8 shows the load-displacement results for each model in each of the three loading directions, where a single direction trend (for example, x) is obtained from averaging the slope of the three sample experiment regressions. The trend lines show the isotropy visually where with the straight-crease model (Figure 8a), the average stiffness trends are separated, but with the parabolic-edge model (Figure 8e), the lines coincide. The representation in Figure 9c offers greater insight into the results as it shows the magnitude of

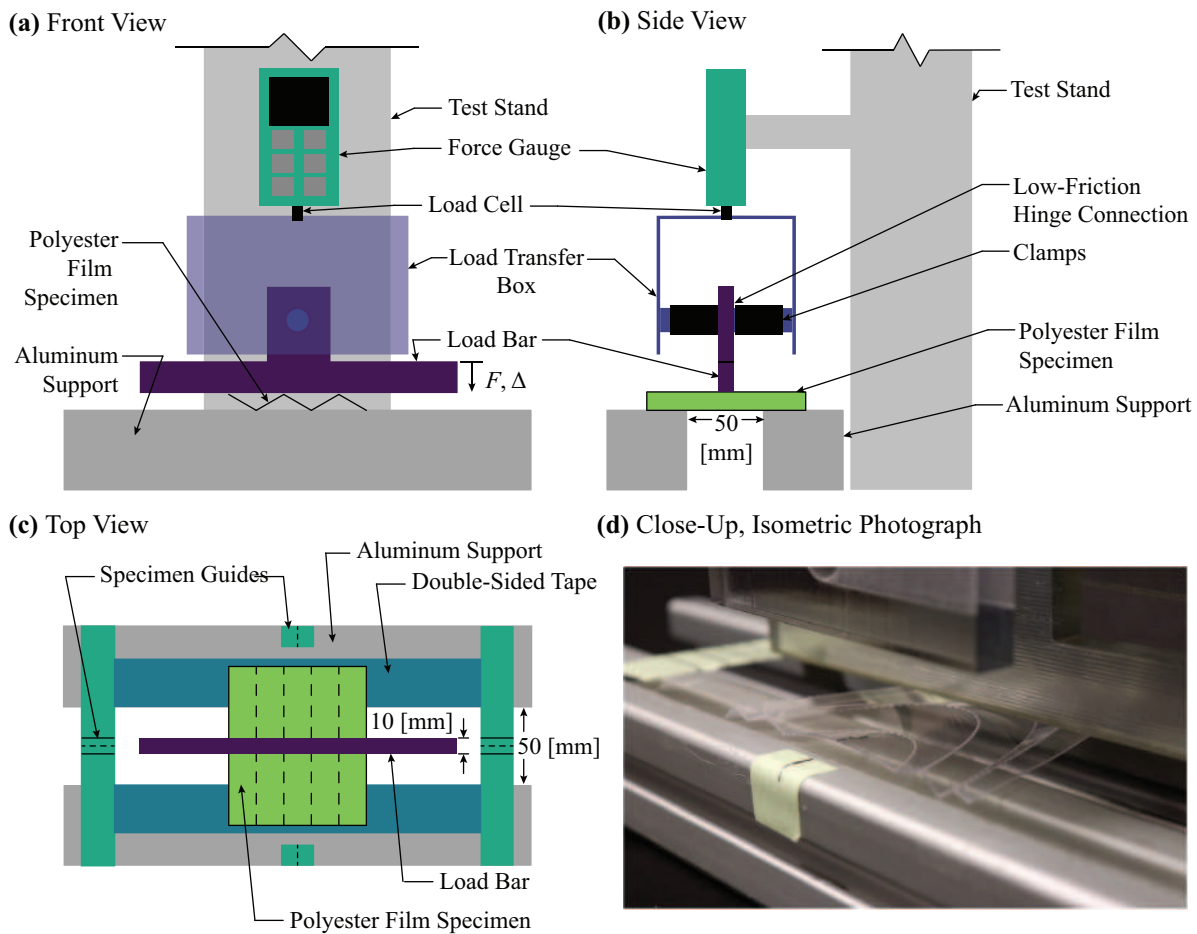


Fig. 6 Experimental setup for three-point bending tests of the corrugations. (a) Front view illustration detailing flow of forces between support, through polyester film specimen, to the force gauge and test stand. (b) Side view illustration showing load bar to load transfer box connection. (c) Top view illustration showing load bar on top of specimen resting on aluminum supports with double-sided tape. (d) Close-up, isometric photograph showing a specimen beneath the load bar.

the stiffness relative to the other specimens. We see that although the parabolic-edge specimen shares similar stiffness in bending about the x -, xy -, and y -directions, the magnitude of the stiffness is less than the maximum magnitude of the straight-crease model. Thus, we say that curved creases “redistribute” stiffness to emphasize the trade-off made when the corrugation’s directionality is no longer uniform. In cases where the corrugation must have a similar bending stiffness in all directions without adding additional members or stiffeners to the structure, curved creases may offer a solution, at the cost of reducing the maximum bending stiffness.

Between the four curved-crease corrugation specimens, we see that the results differ. Namely, the specimens whose flat crease patterns come to a point at the corner give lower stiffness values than the crease patterns that meet at the edge. The point models behave similarly to the straight-crease model in that stiffness in bending about the x -direction is lowest, followed by bending about the xy -direction, with bending about the y -direction being the stiffest. This pattern

between direction stiffness is not maintained for the edge specimens.

5.3 Comparison with theoretical predictions

Next, we compare the bending stiffness predictions made in Section 4 to the experimental results. The values of the top-down procedure (Section 4.2) take an average of the second moment of area, $\bar{I}_{d\perp}$, over the length of the system while the bottom-up procedure (Section 4.3) averages the local second moments of area, I_{loc} . Thus, these approximate predictions do not directly correspond to the experimental, load-deformation stiffness, k , which is computed as a representative value for the bending rigidity of the structure. Like with a tapered beam, this bending stiffness of the corrugations does not directly relate to the average second moment of area of the cross-sections. With this in mind, we can compare the predicted bending stiffness to the experimental results by looking at the magnitudes of the measured values (either $\bar{I}_{d\perp}$,

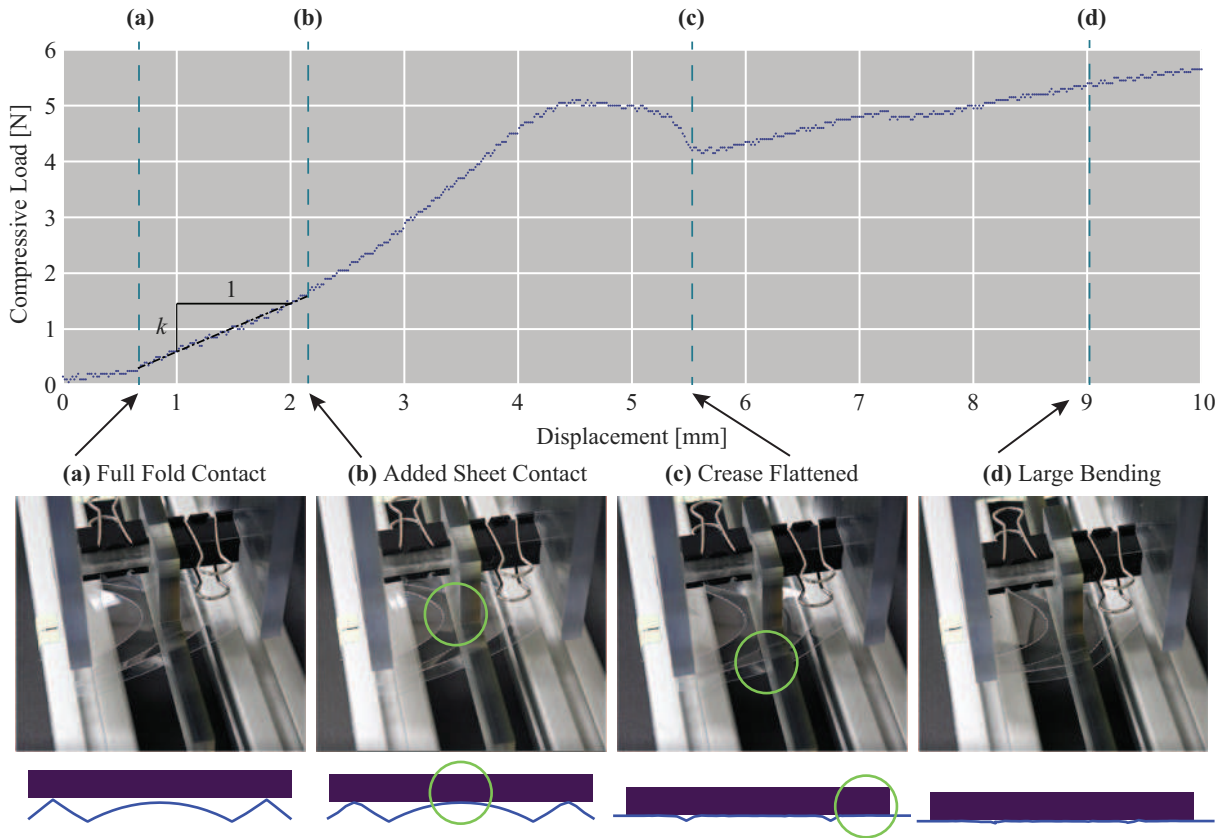


Fig. 7 The process of extracting the corrugation stiffness, k , from the raw load-displacement data starts with moving the load bar downward for a total distance of 10 [mm]. Initially, the load bar only has partial contact with the mountain creases. (a) Once the load bar has full contact with the mountain creases, regression analysis gives the slope of the data (that is, the stiffness). (b) As the specimen continues to deform, additional parts of the sheet come into contact with the load bar. (c) Stiffness becomes negative once the first crease flattens and (d) loading continues with large bending deformations.

I_{loc} , or k) relative to the other bending directions or the other geometries (see Figure 9).

In general, the predictions made by both the bottom-up and top-down procedures predicted the general stiffness relationships well. For the parabolic-point and elliptical-point models, the magnitude of $\bar{I}_{d\perp}$ (Figure 9a) relative to the three bending directions matches the relative magnitude of the average stiffness found in experimental testing (Figure 9c). The relative pattern is also found from the magnitude of I_{loc} (Figure 9b). For the elliptical-edge model, the top-down procedure gave a more accurate prediction of the experimental results when looking at the relative magnitudes of $\bar{I}_{d\perp}$ in all three directions. The bottom-up procedure overestimated the corrugation's ability to resist bending about the xy -direction. For the parabolic-edge model, the bottom-up procedure for calculating I_{loc} gave a better prediction of the relative bending stiffness than the top-down procedure did. However, the bottom-up procedure did overestimate the bending stiffness about the xy -direction.

For both the bottom-up and top-down procedures for predicting bending stiffness of the straight-crease corrugation, the stiffness in the xy - and y -directions was overestimated

compared to the values measured in experimental testing. This overestimation is likely due to the inability of the prediction procedures to incorporate unfolding of the corrugation upon loading. The predictions rest on the assumption that the corrugation will not unfold when loading starts. However, as we observed during loading, the models do unfold as the load bar makes contact with the mountain nodes. With curved-crease corrugations, this effect is less pronounced due to greater crease restriction from other creases surrounding the single crease section, and thus those predictions appear to be better. This discrepancy illustrates the importance of considering all aspects of the qualitative framework, including the properties that cannot be captured from the folded geometry alone (that is, fold restriction and geometric characteristics that reduce unfolding).

Additionally, either method for predicting the bending stiffness of a corrugation from the folded geometry presupposes that the predominant deformation is bending. Although bending plays an essential role in the deformation, torsion within the folded corrugation also contributes to deformations. Both $\bar{I}_{d\perp}$ and I_{loc} fail to capture the ability of the crease to deform in torsion about the crease direction. This

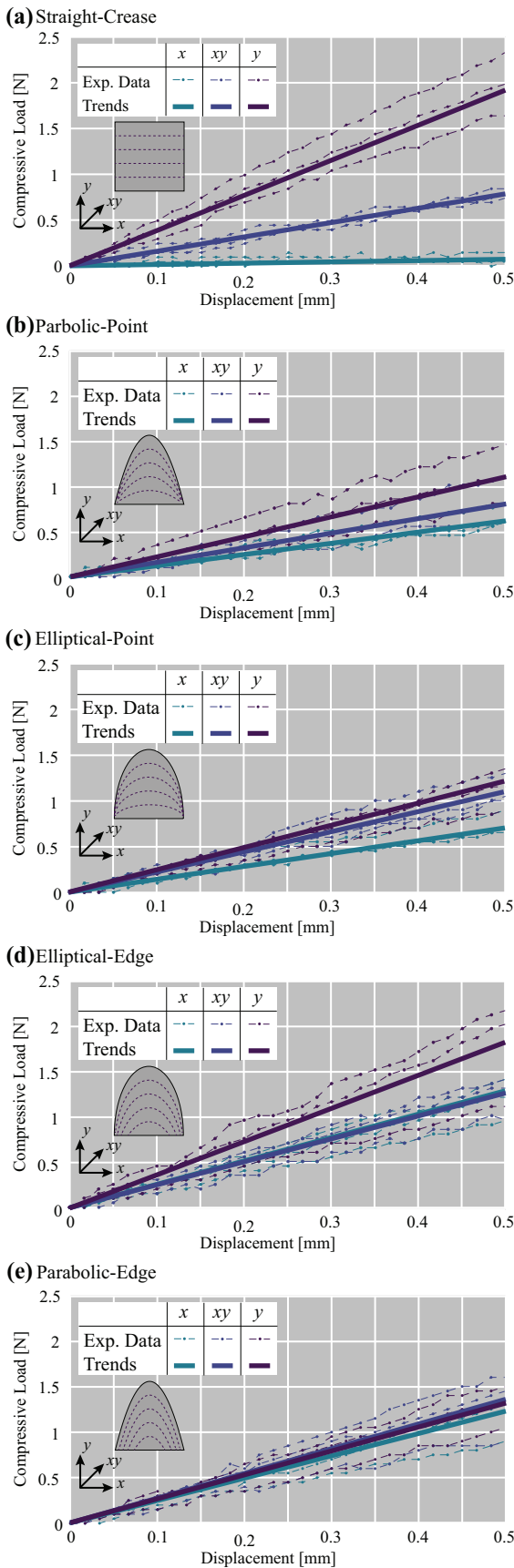


Fig. 8 The load-deformation response of the five models from experimental testing in three directions of bending. Regression analysis on each test is used to calculate the slope (i.e., the stiffness), and the average slope is presented as the trend line. (a) The straight-crease model displays the greatest difference between direction stiffness. (b) The difference significantly narrows with the parabolic-point model and continues with the (c) elliptical-point model and (d) elliptical-edge model. (e) The load-deformation response of the parabolic-edge model shows the most consistent stiffness in all directions – as predicted.

issue, along with the inability to approximate the unfolding behavior, results in these second moment of area estimates to consistently overestimate the actual stiffness of the structure by factors of 3 to 4. For clarity, we do not present these quantitative comparisons here.

Despite these limitations, the methods for predicting bending behavior of a corrugation, either including the full qualitative framework or just the geometric elements, offers a simpler solution than either experimental testing or finite element modeling. The benefits of the top-down and bottom-up procedures start with the benefits of using a simple bar and hinge model to estimate the folded shape. The bar and hinge model can fold corrugations quicker than with a finite element model and is more likely to converge to the desired fold shape. Although the predictions for bending stiffness do not offer an exact mapping to the experimental performance, they offer key insights into the behavior of the corrugation relative to other crease patterns with a simple values (such as I_{loc}). In cases where a pattern must be chosen to accomplish some goal (for instance, having a similar bending stiffness in all directions in the xy -plane), designs can be compared quickly as prototypes. The final design can be modeled with greater fidelity in a finite elements program to better account for torsional and fold restriction effects.

6 Conclusions and future work

In this paper, we introduced and explored corrugations with curved creases which are unique because they have a high bending stiffness in multiple directions. We then presented a theoretical framework and two predictive methods that use the geometry of a corrugation to qualitatively estimate its stiffness characteristics. Experimental data verified the multi-directional bending stiffness of corrugations, and confirmed the validity of the predictive methods.

We offered a theoretical, qualitative framework for relating the bending stiffness of a corrugation to its geometric properties at four scales: (1) sheet sections, (2) unit cross-sections, (3) single creased sheets, and (4) the corrugation system. The framework suggests that the depth of creases, the ability of the system to resist flattening, the curvature and orientation of curved creases, and the different variety of crease geometries in a corrugation are all important char-

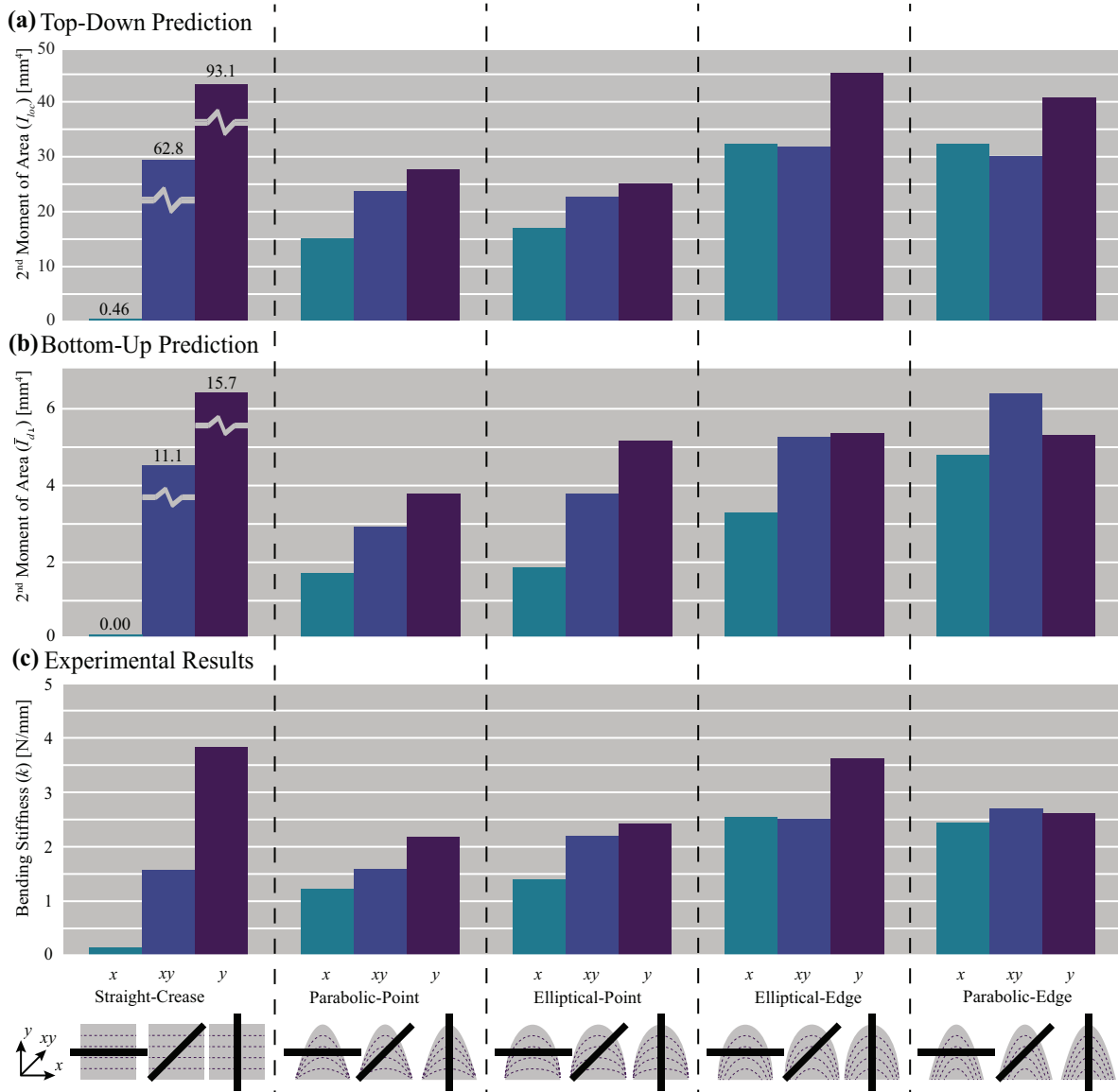


Fig. 9 A comparison between the theoretical bending stiffness predictions and the experimental results in the x -, xy -, and y -directions for each of the five models. The prediction methods, (a) top-down and (b) bottom-up, use different averages for the second moments of area about directions in the xy -plane as a proxy for bending stiffness. The shapes of the bars in (c) the experimental results corresponds to the shapes of the bars in the prediction results, suggesting that second moment of area is proportional to the bending stiffness, with errors stemming from the limitations of each prediction method.

acteristics influencing the stiffness. This framework allows a designer to make a rough estimate of the bending stiffness and identify issues with a corrugation by looking at the folded geometry.

We also offered two methods to predict the bending stiffness of a corrugation by analyzing the geometry that is simulated by a bar and hinge model. Both methods make an approximation of the second moment of area within the corrugation geometry. The top-down method approaches the problem globally by looking at the entire cross-section at different points along the span of the corrugation. The bottom-up method looks locally at the orientation of crease segments

and evaluates their contribution for different directions of bending.

We analyzed five example corrugations, where one was a straight-crease pattern and four had different curved-crease designs. The two predictive methods gave similar results to each other, and identified differences between the corrugation designs. We then validated the theoretical framework and predictive model using experimental three-point bending tests on polyester film specimens of the example corrugation. We found that the theoretical frameworks effectively estimated the relative magnitude of the bending stiffness for each model in the x -, xy -, and y -directions. There were small

deviations attributed to the fact that the quantitative framework cannot capture certain features of the corrugation, such as fold stiffness and boundary restraints on the structure. Each method showed that traditional, v-shaped corrugations made with straight creases have stiffness anisotropy, while the curved-crease corrugations are stiff in multiple directions. Additionally, patterns where curved creases intersected one edge gave higher bending stiffness than patterns where creases coincide at the corners.

This work is a starting point for future research on the conception, analysis, or design of curved-crease corrugations with novel mechanical properties. The proposed framework can predict corrugation stiffness, but could be further improved to include the influence of boundary conditions and flattening of the creases during loading. The multi-directional stiffness of the curved-crease corrugations can be reasonably explained by the diverse directionality of creases; however, it would be worthwhile for future work to explain exactly how these corrugations resist bending and torsional deformations. Insight to the stress distribution and load paths within the corrugation can give a more elegant explanation to the local mechanics responsible for the unique multi-directional stiffness. Additionally, further investigation into the influence of the Poisson's effect within the corrugation would improve the accuracy of these findings for a more thorough mechanical treatment of curved-crease corrugations.

The corrugation geometries that we have presented in this work were developed through trial and error, and were refined based on our geometric framework in Section 2. However, many variations are possible with curved-crease geometries, and it would be helpful to systematically explore these through parametric studies (for example, number of creases, curvatures, spacings, etc.). These studies could be further extended to perform optimization of the stiffness, anisotropy, or shape of the pattern. Additionally, understanding the predominant stiffness of nonplanar-midsurface corrugations could begin by using the insights found in our investigation of planar-midsurface corrugations with the addition of predicting the torsional and shear stiffness. Finally, future work is needed to explore practical applications of the curved-crease corrugations in both conventional applications such as stiff decking or in emerging applications such as morphing or multi-functional structures. This article sets an important starting point for analyzing general corrugations, including curved-crease corrugations, by offering qualitative and quantitative methods for analyzing the structures relative to other designs. We hope that further research into the topic will expand the scope of our knowledge and allow for a complete understanding of the bending behavior, including a theoretically or empirically verified mapping between the average second moments of area and the bending stiffness.

Our methods for describing the bending stiffness of corrugations offers a way for engineers to design for isotropy

of bending stiffness by visually analyzing the folded pattern and running quick folding simulations using a simple bar and hinge model. This process does not require complex finite element simulations, which from our experience, can be difficult to carry out for curved-crease folding patterns. These new methods have the possibility of connecting the form of curved-crease origami to its function in a variety of applications that require continuous, lightweight sheets as structural members.

Acknowledgements We thank Jack Riley (University of Michigan) for his preliminary experimental work on curved parabolas that verified their unique characteristics and fueled our curiosity for curved-crease corrugations, as a whole.

Conflict of interest

The authors declare that they have no conflict of interest.

Appendix A: Details on the crease pattern geometries

In this appendix, we give the specific functions used to generate the flat crease patterns shown in Figure 3. We also present the values we used in the functions so that our results can be further examined or replicated. Note that for each of the five geometries, $W = 100$ [mm], $H = 100$ [mm], $n_s = 5$, and $i \in \{1, 2, 3, 4, 5\}$.

Straight-crease corrugation For the straight-crease corrugation, there is one input besides the constraining assumptions: a_i . The function defining the i^{th} curve of the crease pattern is,

$$y_i = a_i, \quad (11)$$

where,

$$a_i = \frac{H}{n_s} i. \quad (12)$$

The functions are defined in the domain $-W/2 \leq x \leq W/2$. An example crease pattern used in the analyses and experimentation is shown in Figure 3a with corresponding parameter values in Table 1.

Parabolic-point corrugation For the parabolic-point corrugation, there are two inputs besides the constraining assumptions: b_i and c_i . The function defining the i^{th} curve is,

$$y_i = b_i x_i^2 + c_i, \quad (13)$$

where,

$$c_i = \frac{H}{n_s} i; \quad b_i = -\frac{4c_i}{W^2} = -\frac{4H}{W^2 n_s} i. \quad (14)$$

The functions are defined in the domain $-r_i \leq x_i \leq r_i$, where $r_i = \sqrt{-c_i/b_i} = W/2$. An example crease pattern is shown in Figure 3b with corresponding values in Table 2.

Table 1 Geometric parameter values for example straight-crease pattern (see Figure 3a).

$y_i = a_i, \quad -r_i \leq x_i \leq r_i$		
i	a_i [mm]	r_i [mm]
1	20.0	50.0
2	40.0	50.0
3	60.0	50.0
4	80.0	50.0
5	100	50.0

Table 2 Geometric parameter values for example parabolic-point pattern (see Figure 3b).

$y_i = b_i x_i^2 + c_i, \quad -r_i \leq x_i \leq r_i$			
i	b_i [mm ⁻¹]	c_i [mm]	r_i [mm]
1	-0.008	20.0	50.0
2	-0.016	40.0	50.0
3	-0.024	60.0	50.0
4	-0.032	80.0	50.0
5	-0.040	100	50.0

Table 3 Geometric parameter values for example parabolic-edge pattern (see Figure 3c).

$y_i = b_i x_i^2 + c_i, \quad -r_i \leq x_i \leq r_i$			
i	b_i [mm ⁻¹]	c_i [mm]	r_i [mm]
1	-0.040	20.0	22.4
2	-0.040	40.0	31.6
3	-0.040	60.0	38.7
4	-0.040	80.0	44.7
5	-0.040	100	50.0

Parabolic-edge corrugation For the parabolic-edge corrugation, two inputs additional inputs are required: b_i and c_i . The function defining the i^{th} curve is,

$$y_i = b_i x_i^2 + c_i, \quad (15)$$

where,

$$b_i = -\frac{4H}{W^2}; \quad c_i = \frac{H}{n_s} i. \quad (16)$$

Each curve is defined in the domain $-r_i \leq x \leq r_i$, where $r_i = \sqrt{-c_i/b_i} = \sqrt{W^2 i / (4n_s)}$. An example crease pattern is shown in Figure 3c with corresponding values in Table 3

Elliptical-point corrugation For the elliptical-point corrugation, three inputs besides the constraining assumptions are required: d_i , e_i , and f_i . The function defining the i^{th} curve is,

$$y_i = e_i \sqrt{1 - \left(\frac{x_i}{d_i}\right)^2} + f_i, \quad (17)$$

Table 4 Geometric parameter values for example elliptical-point pattern (see Figure 3d).

$y_i = e_i \sqrt{1 - (x_i/d_i)^2} + f_i, \quad -r_i \leq x_i \leq r_i$				
i	d_i [mm]	e_i [mm]	f_i [mm]	r_i [mm]
1	50.0	20.0	0.00	50.0
2	50.0	40.0	0.00	50.0
3	50.0	60.0	0.00	50.0
4	50.0	80.0	0.00	50.0
5	50.0	100	0.00	50.0

Table 5 Geometric parameter values for example elliptical-edge pattern (see Figure 3e).

$y_i = e_i \sqrt{1 - (x_i/d_i)^2} + f_i, \quad -r_i \leq x_i \leq r_i$				
i	d_i [mm]	e_i [mm]	f_i [mm]	r_i [mm]
1	50.0	100	-80.0	30.0
2	50.0	100	-60.0	40.0
3	50.0	100	-40.0	45.8
4	50.0	100	-20.0	49.0
5	50.0	100	0.00	50.0

where,

$$d_i = \frac{W}{2}; \quad e_i = \frac{H}{n_s} i; \quad f_i = 0. \quad (18)$$

Each curve is defined in the domain $-r_i \leq x_i \leq r_i$, where $r_i = d_i \sqrt{1 - (-f_i/e_i)^2} = W/2$. An example crease pattern is shown in Figure 3d with corresponding values in Table 4.

Elliptical-edge corrugation For the elliptical-edge corrugation, three inputs are required besides the constraining assumptions: d_i , e_i , and f_i . The function defining the i^{th} curve is,

$$y_i = e_i \sqrt{1 - \left(\frac{x_i}{d_i}\right)^2} + f_i, \quad (19)$$

where,

$$d_i = \frac{W}{2}; \quad e_i = H; \quad f_i = H \left(\frac{i}{n_s} - 1\right). \quad (20)$$

Each curve is defined in the domain $-r_i \leq x_i \leq r_i$, where $r_i = d_i \sqrt{1 - (-f_i/e_i)^2} = W/2 \sqrt{2i/n_s - (i/n_s)^2}$. An example crease pattern is shown in Figure 3e with corresponding values in Table 5.

References

1. Badger, J.C., Nelson, T.G., Lang, R.J., Halverson, D.M., Howell, L.L.: Normalized Coordinate Equations and an Energy Method for Predicting Natural Curved-Fold Configurations. *Journal of Applied Mechanics* **86**(7) (2019). DOI 10.1115/1.4043285

2. Bouaziz, O.: Geometrically induced strain hardening. *Scripta Materialia* **68**(1), 28–30 (2013). DOI 10.1016/j.scriptamat.2012.08.008
3. Dayyani, I., Shaw, A.D., Saavedra Flores, E.I., Friswell, M.I.: The mechanics of composite corrugated structures: A review with applications in morphing aircraft. *Composite Structures* **133**, 358–380 (2015). DOI 10.1016/j.compstruct.2015.07.099
4. Demaine, E.D., Demaine, M.L., Koschitz, D., Tachi, T.: Curved crease folding – a review on art, design and mathematics. In: *Proceedings of the IABSE-IASS Symposium: Taller, Longer, Lighter* (2011)
5. Duncan, J.P., Duncan, J.L.: Folded developables. *Proceedings of the Royal Society of London. Series A, Mathematical and Physical Sciences* **383**(1784), 191–205 (1982)
6. Filipov, E.T., Liu, K., Tachi, T., Schenk, M., Paulino, G.H.: Bar and hinge models for scalable analysis of origami. *International Journal of Solids and Structures* **124**, 26–45 (2017). DOI 10.1016/j.ijsolstr.2017.05.028
7. Filipov, E.T., Tachi, T., Paulino, G.H.: Origami tubes assembled into stiff, yet reconfigurable structures and metamaterials. *Proceedings of the National Academy of Sciences of the United States of America* **112**(40), 12321–12326 (2015). DOI 10.1073/pnas.1509465112
8. Fraser, M., Zurob, H.S., Wu, P.: Comparing the effect of geometry on the stress-strain response of isolated corrugation structures and corrugation reinforced composite structures. *Composite Structures* **187**, 308–315 (2018). DOI 10.1016/j.compstruct.2017.12.076
9. Gattas, J.M., Lv, W., Chen, Y.: Rigid-foldable tubular arches. *Engineering Structures* **145**, 246–253 (2017). DOI 10.1016/j.engstruct.2017.04.037
10. Gattas, J.M., You, Z.: The behaviour of curved-crease foldcores under low-velocity impact loads. *International Journal of Solids and Structures* **53**, 80–91 (2015). DOI 10.1016/j.ijsolstr.2014.10.019
11. Gholamhoseini, A., Khanlou, A., MacRae, G., Hicks, S., Scott, A., Clifton, C.: Short-term behaviour of reinforced and steel fibre-reinforced concrete composite slabs with steel decking under negative bending moment. *Advances in Structural Engineering* **21**(9), 1288–1301 (2018). DOI 10.1177/1369433217739710
12. Gilewski, W., Pełczyński, J., Stawarz, P.: A comparative study of origami inspired folded plates. *Procedia Engineering* **91**, 220–225 (2014). DOI 10.1016/j.proeng.2014.12.050
13. Gracias, D.H., Kavthekar, V., Love, J.C., Paul, K.E., Whitesides, G.M.: Fabrication of micrometer-scale, patterned polyhedra by self-assembly. *Advanced Materials* **14**(3), 235–238 (2002)
14. Huffman, D.A.: Curvature and creases: A primer on paper. *IEEE Transactions on Computers* **C-25**(10), 1010–1019 (1976). DOI 10.1109/TC.1976.1674542
15. Ketchum, M.S.: Design and construction of a folded plate roof structure. *ACI Journal Proceedings* **51**(1), 449–456 (1955). DOI 10.14359/11688
16. Klett, Y., Middendorf, P., Sobek, W., Haase, W., Heidingsfeld, M.: Potential of origami-based shell elements as next-generation envelope components. In: *2017 IEEE International Conference on Advanced Intelligent Mechatronics (AIM)*, pp. 916–920 (2017). DOI 10.1109/AIM.2017.8014135
17. Klett, Y., Zeger, C., Middendorf, P.: Experimental characterization of pressure loss caused by flow through foldcore sandwich structures. *American Society of Mechanical Engineers Digital Collection* (2017). DOI 10.1115/DETC2017-67890
18. Lang, R.J., Nelson, T.G., Magleby, S.P., Howell, L.L.: Kinematics and discretization of curved-fold mechanisms. In: *Proceedings of the ASME 2017*. ASME (2017). DOI 10.1115/DETC2017-67439
19. Lechenault, F., Thiria, B., Adda-Bedia, M.: Mechanical response of a creased sheet. *Physical Review Letters* **112**(24), 244301 (2014). DOI 10.1103/PhysRevLett.112.244301
20. Lee, T.U., You, Z., Gattas, J.M.: Elastic surface generation of curved-crease origami. *International Journal of Solids and Structures* **136–137**, 13–27 (2018). DOI 10.1016/j.ijsolstr.2017.11.029
21. Liu, K., Paulino, G.H.: Nonlinear mechanics of non-rigid origami: an efficient computational approach. *Proceedings of the Royal Society A: Mathematical, Physical and Engineering Sciences* **473**(2206), 20170348 (2017). DOI 10.1098/rspa.2017.0348
22. Mahadevan, L., Rica, S.: Self-Organized Origami. *Science* **307**(5716), 1740–1740 (2005)
23. Norman, A.D., Seffen, K.A., Guest, S.D.: Multistable corrugated shells. *Proceedings of the Royal Society A: Mathematical, Physical and Engineering Sciences* **464**(2095), 1653–1672 (2008). DOI 10.1098/rspa.2007.0216
24. Norman, A.D., Seffen, K.A., Guest, S.D.: Morphing of curved corrugated shells. *International Journal of Solids and Structures* **46**(7), 1624–1633 (2009). DOI 10.1016/j.ijsolstr.2008.12.009
25. Schenk, M., Guest, S.D.: Origami folding: A structural engineering approach. In: P. Wang-Iverson, R.J. Lang, M. Yim (eds.) *Origami 5: Fifth International Meeting of Origami Science, Mathematics, and Education*, 1 edn., pp. 291–303. A K Peters/CRC Press (2011)
26. Seong, D.Y., Jung, C.G., Yang, D.Y., Moon, K.J., Ahn, D.G.: Quasi-isotropic bending responses of metallic sandwich plates with bi-directionally corrugated cores. *Materials and Design* **31**(6), 2804–2812 (2010). DOI 10.1016/j.matdes.2010.01.009
27. Thill, C., Etches, J.A., Bond, I.P., Potter, K.D., Weaver, P.M.: Composite corrugated structures for morphing wing skin applications. *Smart Materials and Structures* **19**(12), 124009 (2010). DOI 10.1088/0964-1726/19/12/124009
28. Timoshenko, S., Woinowsky-Krieger, S.: *Theory of Plates and Shells*, 2nd edn. McGraw-Hill, New York (1959)
29. Vergauwen, A., Laet, L.D., Temmerman, N.D.: Computational modelling methods for pliable structures based on curved-line folding. *Computer-Aided Design* **83**, 51–63 (2017). DOI 10.1016/j.cad.2016.10.002
30. Woodruff, S.R., Filipov, E.T.: Structural analysis of curved folded deployables. In: *Earth and Space 2018*, pp. 793–803. ASCE (2018). DOI 10.1061/9780784481899.075
31. Woodruff, S.R., Filipov, E.T.: A bar and hinge model formulation for structural analysis of curved-crease origami. (Submitted) (2020)
32. Zhang, Z., Qiu, T., Song, R., Sun, Y.: Nonlinear finite element analysis of the fluted corrugated sheet in the corrugated cardboard. *Advances in Materials Science and Engineering* **2014**, 654012 (2014). DOI <https://doi.org/10.1155/2014/654012>